DOI: https://doi.org/10.54966/jreen.v28i2.1490

Journal of Renewable Energies

Revue des Energies Renouvelables

Journal home page: https://revue.cder.dz/index.php/rer

Research paper

Control Design and Experimental Validation of a Scalable Single-Phase Islanded AC Microgrid Testbed for Research and Education

Abderrezzaq Bouharchouche [a,b,*], El Madjid Berkouk [a], Walid R. Issa [c], Abderezak Lashab [d], Abdelhamid Kaabeche [b], Josep M. Guerrero [d]

[a] *LCP Laboratory, Ecole Nationale Polytechnique d'Alger, Avenue Hacen Badi El harrach, Algiers 16200, Algeria*

[b] *Centre de Développement des Energies Renouvelables, CDER, BP 62 Route de l'Observatoire, Bouzaréah, 16340, Algiers, Algeria*

[c] *Electrical Engineering Department, Sheffield Hallam University, Pond Street, Sheffield S1 1WB, UK*

[d] *Center for Research on Microgrids (CROM), AAU Energy, Aalborg University, 9220, Aalborg, Denmark*

ARTICLE INFO

Article history:

Received July 22, 2025

Accepted November 4, 2025

Available online Nov 24, 2025

Published December 14, 2025

Keywords:

Islanded AC Microgrid,
Hierarchical Control,
Experimental Testbed,
Educational Microgrid,
Distributed Generator.

ABSTRACT

This paper presents a research and educational tool for islanded AC microgrids. High penetration of renewable energy can cause instability in traditional power grids. Microgrid technology addresses this by effectively integrating local renewable sources, managing energy through intelligent coordination, and can support the main power grid. However, obtaining test beds for research and education remains challenging due to system complexity, cost, and limited scalability in existing solutions. In this paper, the hierarchical control design of an islanded AC microgrid, which includes inner loop Proportional-Resonant controllers for voltage regulation, Phase-Locked Loop-based synchronization, virtual impedance for decoupling active and reactive powers, droop control for power sharing, and a secondary controller for voltage and frequency restoration as well as reactive power compensation is detailed. The experimental setup consists of two distributed generators (inverters) feeding linear and nonlinear loads. It is controlled by a dSPACE platform, with STMF4 Discovery microcontrollers generating Pulse-Width-Modulation signals to reduce the computational burden on dSPACE and facilitate scalability. Experimental results demonstrate that the testbed maintains stable operation under various load conditions, achieves proper power sharing, and restores the microgrid's frequency and voltage to predefined levels. Its modular design supports future expansion for both research and teaching, enabling hands-on experimentation and analysis.

* *Corresponding author, E-mail address: abderrezzaq.bouharchouche@g.enp.edu.dz*
Tel : + 213 552917648

ISSN: 1112-2242 / EISSN: 2716-8247

This work is licensed under a Creative Commons Attribution-NonCommercial-ShareAlike 4.0 International License.

1. INTRODUCTION

The electrical power systems are undergoing a significant shift toward decentralization and decarbonization. Motivated by increased electrification as the society is moving toward a more "electrical everything" future, and the need to integrate renewable energy sources (RES) like solar and wind to combat climate change. Thus, electricity networks are moving away from centralized fossil generation toward distributed renewable resources (DERs) (Hirsch et al., 2018). With high penetration levels of RES into existing grids presents significant challenges related to intermittency, variability, and grid stability (Daneshvar et al., 2021).

In this context, microgrids have emerged as a flexible way to integrate diverse DERs at the local level (Hirsch et al., 2018). Defined as localized energy systems that integrate multiple distributed generators (e.g., solar panels, wind turbines), energy storage systems (e.g., batteries), and various loads, operating in a coordinated manner to manage energy flow intelligently. They can function in islanded mode, disconnected from the main grid, or in grid-connected mode, providing services such as black start, reactive power compensation, and voltage regulation (Guerrero et al., 2011). Their role in integrating renewable energy with high penetration is essential, as they enable decentralized generation, reduce transmission losses, and support grid stability during outages (Quizhpe et al., 2024). Moreover, these features make microgrids attractive for critical infrastructure and remote communities (Rodriguez-Martinez et al., 2023).

However, deploying microgrids also raises complex control challenges, especially in islanded operation. Unlike a stiff grid, an islanded microgrid must maintain voltage and frequency by internal means. A common approach is droop control, where each inverter adjusts its output frequency and voltage amplitude in proportion to active and reactive power output (Govind et al., 2023). To achieve accurate power sharing and maintain stability, droop controllers are often enhanced with virtual impedance methods and advanced voltage controllers (Buraimoh et al., 2022). Additionally, virtual impedance is utilized for soft-start procedures, harmonic mitigation, and to enhance overall system robustness and stability (Prasad & Parimi, 2023). To restore the frequency and the voltage amplitude of the microgrid to their nominal values, a secondary control layer is used, which is part of a hierarchical control structure, operating on a slower time scale than the primary control, which integrates inner control loops and the droop mechanism (Khayat et al., 2020). Secondary control generally requires communication among generators; thus, ensuring a reliable, fault-tolerant communication network is a key concern. Distributed or peer-to-peer control architectures have been proposed to improve robustness by avoiding single points of failure (Chakraborty et al., 2024; Lian et al., 2023).

Given these multifaceted challenges, hardware testbeds have become indispensable tools for advancing research and education in microgrid technology (He et al., 2022). Although, advanced simulation software tools such as XENDEE and HOMER-PRO could provide powerful capabilities for the design, sizing, and optimization of microgrids (Uddin et al., 2023), this study does not focus on software optimization or power-flow analysis. Despite their importance, existing experimental microgrid setups face significant challenges, including complexity, high cost, and limited reproducibility (Lidula & Rajapakse, 2011). For instance, the Oak Ridge National Laboratory built an advanced microgrid testbed that uses 480 V three-phase systems and high-end controllers to simulate real microgrid operations (Ferrari et al., 2024). Although it is very modern and powerful, this kind of setup is too expensive and complex for most universities or research labs to use for teaching or experiments. To bridge this gap, recent work has developed laboratory-scale microgrid platforms. Haidekker et al. (2023) introduced a low-voltage (12 V AC) tabletop AC microgrid with modular inverter and load units. This system allows students to safely test things like frequency, phase, and power sharing. Their SmartGridLab shows that low-cost and flexible microgrids can work in classrooms, but they also reveal some challenges: these

setups can still be hard to build, require expensive hardware, and may not scale well if more generators are added. Uddin et al. (2023) point out that inconsistent regulations and policies make it hard to replicate microgrid setups, especially in developing countries. This makes it tough for smaller institutions and educational programs to use these setups, limiting their widespread use (Wang R. et al., 2020).

To address these issues, we propose in this work a low-cost, scalable, single-phase islanded microgrid testbed suitable for both research and education. To the best of the authors' knowledge, the proposed experimental architecture for a single-phase islanded AC microgrid testbed is novel. The main contributions of this paper can be summarized as follows:

- A modular experimental architecture for the microgrid is proposed, which allows easy expansion for additional distributed generators.
- Low-cost STM32F4 Discovery microcontroller boards are used to generate PWM signals for each inverter in order to reduce the computational load on the main dSPACE platform.
- The design methodology of the key microgrid hierarchical control strategies (droop control, virtual impedance, and secondary voltage restoration) is presented to help students and researchers understand, reproduce, and implement similar setups.
- Experimental results are provided to demonstrate the performance of the proposed testbed.
- The proposed architecture balances simplicity, cost, and functionality, making it suitable for laboratories and educational systems with limited resources.

The remainder of this paper is organized as follows. Section 2 describes the single-phase islanded microgrid testbed under study. Section 3 presents the development of primary and secondary control algorithms for voltage regulation and power sharing. Section 4 reports experimental results and analyzes the system's performance under different conditions. Finally, Section 5 summarizes the conclusions and contributions of this work.

2. SYSTEM DESCRIPTION

In this work, we propose a novel experimental architecture for a single-phase islanded AC microgrid testbed dedicated to research and education. The microgrid setup consists of two distributed generators (DGs) powered by a DC bus, representing a renewable energy source combined with an energy storage system to enhance dispatchability, as depicted in Fig. (1). LC filters are integrated at the inverter outputs to mitigate high-order harmonics and stabilize the voltage. These two DGs are connected to a common bus, known as the Point of Common Coupling (PCC). The system accommodates both linear and nonlinear loads connected to the PCC, with the nonlinear loads implemented using a single-phase diode bridge rectifier coupled with a complex RC impedance.

Current and voltage acquisition boards were developed using LA55P current sensor and LV25P voltage sensor, respectively. Additionally, two isolation and adaptation boards were realized based on optocouplers (4N25) to generate 15 V level PWM signals for the inverter drivers, ensuring proper isolation between the control circuit and the power circuit. This isolation boards gets the PWM signals for each inverter from two different STM32F4 Discovery boards, which are considered as budget-friendly yet capable microcontrollers. This development boards were programmed using the Waijung 17.03a Toolbox, an open-source tool that integrates directly with Simulink. This toolbox was used to generate PWM signals, which are subsequently employed to control the inverter, thereby relieving the dSPACE system from this task and consequently reducing the computational burden.

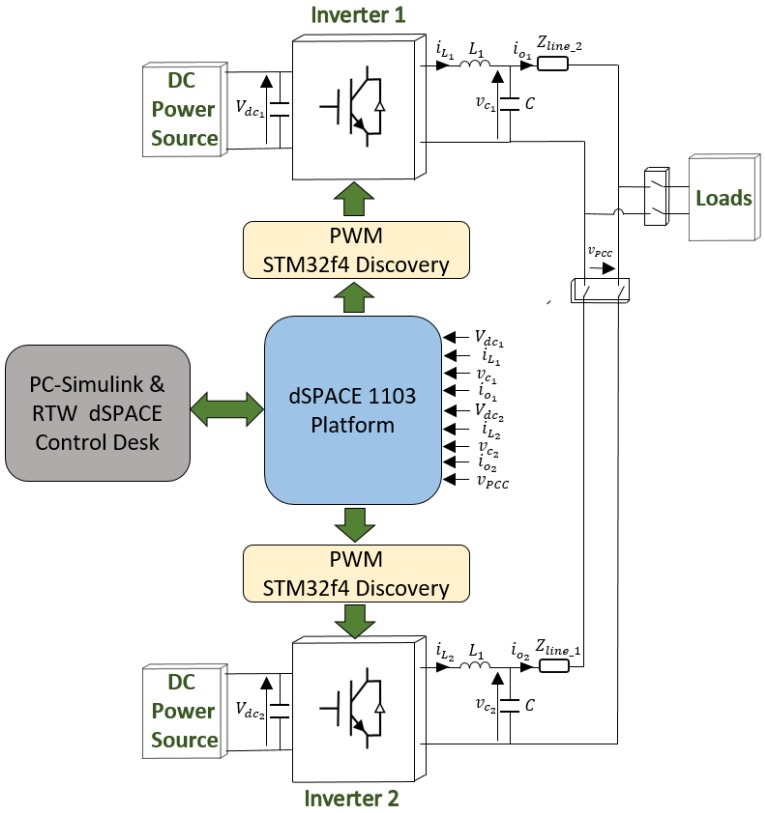

Fig 1. Schematic of the experimental microgrid setup.

3. CONTROL STRATEGY

The control of this AC microgrid is based on the hierarchical control architecture, as shown in Figure 2. In this paper, tertiary control is not addressed, as it focuses more on energy management and planning in the mid- and long-term (Guerrero et al., 2011). As described in Fig. (2), each control level operates on a different time scale. The closer the control level is to the inverter, the higher the bandwidth becomes, resulting in a faster controller response (Shrivastava & Subudhi, 2020).

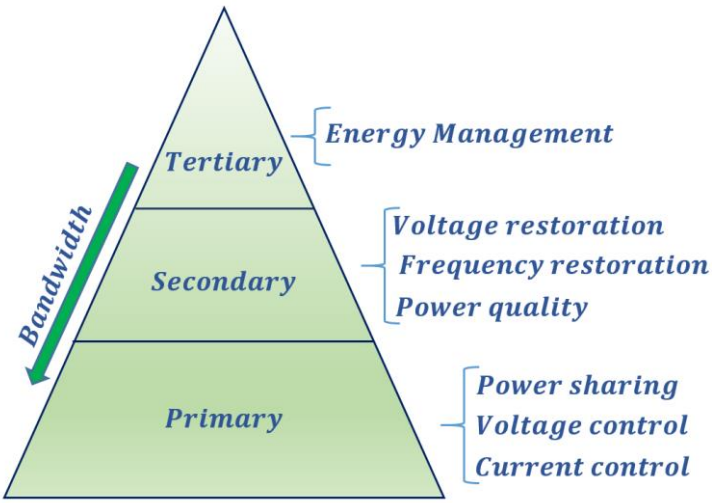

Fig 2. General scheme of the hierarchical control in islanded microgrids.

Figure (3) presents the overall hierarchical control strategy for the studied single-phase islanded AC microgrid. The measurement acquisition and control calculations are performed by the dSPACE1103 platform, and the duty cycle references are sent to two STM32F4 Discovery boards to generate the PWM signals for each inverter, enabling a modular structure that can integrate additional distributed generators.

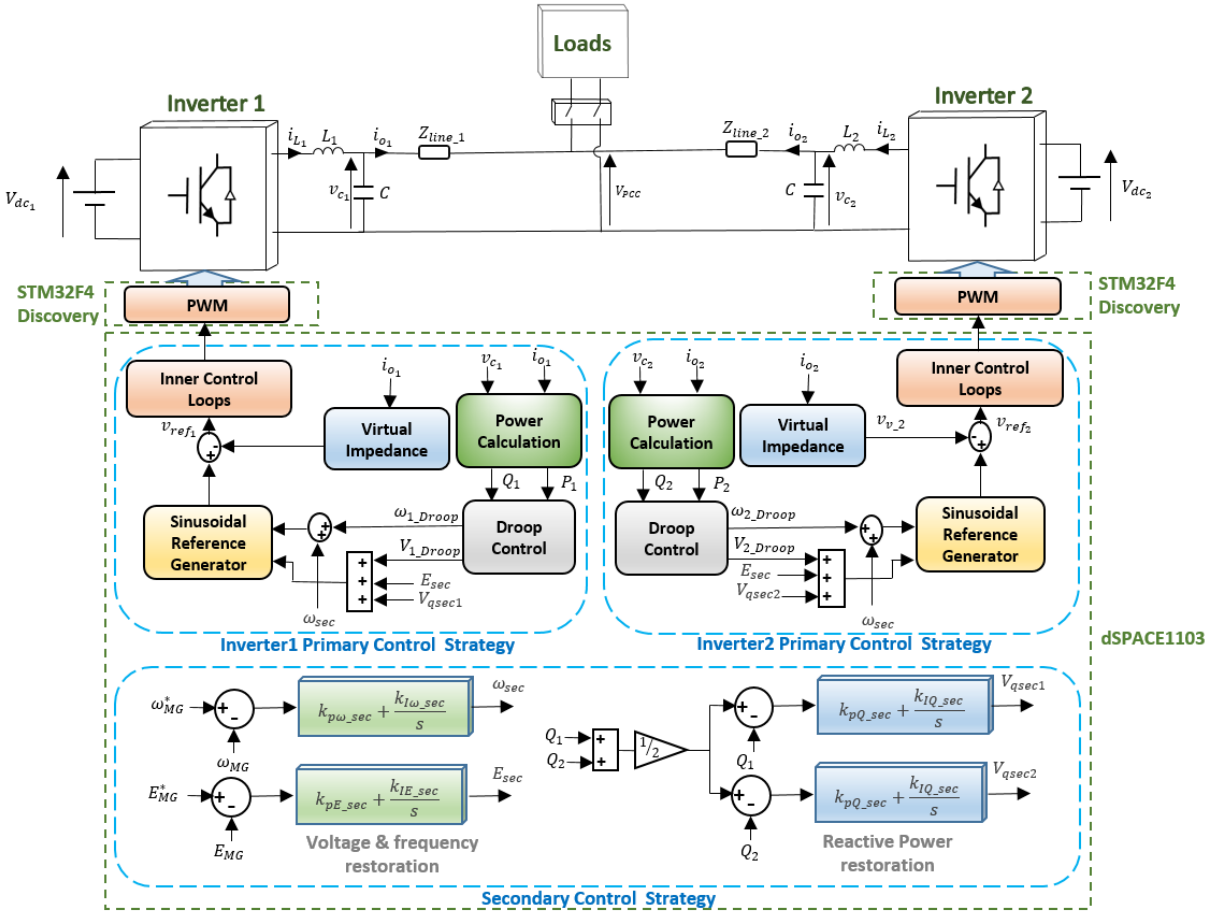

Fig.3. Overall control strategy of the single-phase islanded AC microgrid experimental setup.

3.1 Inner Control Loops

The voltage reference V_{ref}, generated by the upper control levels of the hierarchical strategy, is transmitted to the inner control loops. These loops consist of a cascaded structure: an outer voltage control loop and an inner current control loop as shown in Fig. (4). The purpose of the inner loops is to regulate the inverter's output current flowing through the filter inductance, as well as the voltage across the filter capacitor in the LC filter. Proportional-Resonant (PR) controllers are employed in both loops due to their effectiveness in tracking sinusoidal references with zero steady-state error (Vasquez et al., 2013). The PR controller structure used is expressed as follows:

$$G_v(s) = k_{p_V} + \frac{k_{r_V}\, s}{s^2 + 2\,\omega_c s + \omega_0^2} \tag{1}$$

$$G_i(s) = k_{p_I} + \frac{k_{r_I}\, s}{s^2 + 2\,\omega_c s + \omega_0^2} \tag{2}$$

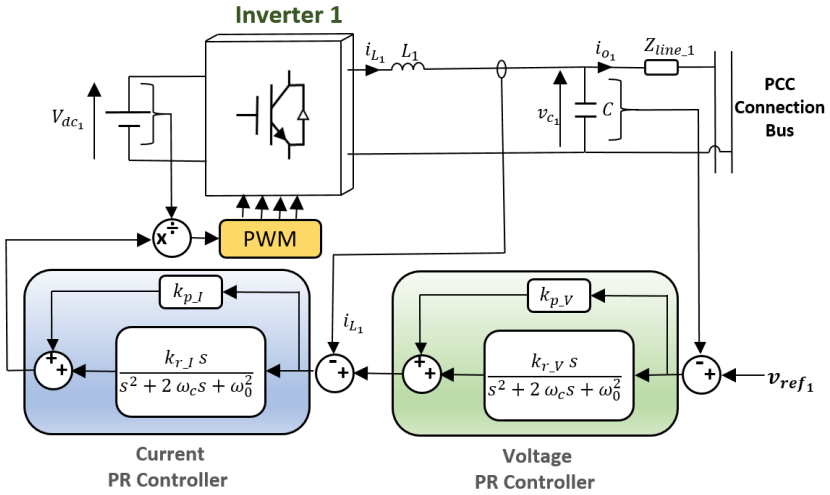

Fig 4. The inner voltage and current loops.

The block diagram of the single-phase inverter is depicted in Fig. (5), where $G_{PWM}(s)$ is a delay element representing the PWM Inverter block, which includes sampling and transport delays between the control and the plant. The sampling delay equals one sampling period T_s, and the transport delay is modeled as $0.5T_s$ (Sreekumar & Khadkikar, 2017). Thus, we can write:

$$G_{PWM}(s) = \frac{1}{1 + 1.5s} \tag{3}$$

We have applied Mason's theorem for block reduction and derived the following equation:

$$v_{c1}(s) = \frac{G_v(s)G_i(s)G_{PWM}(s)}{LCs^2 + RCs + \big(Cs + G_v(s)\big)G_i(s)G_{PWM}(s) + 1} v_{ref1}(s) - \frac{Ls + G_i(s)G_{PWM}(s)}{LCs^2 + RCs + \big(Cs + G_v(s)\big)G_i(s)G_{PWM}(s) + 1} i_{o1}(s) \tag{4}$$

This is represented in the form:

$$v_{c1}(s) = G_{cl}(s)\, v_{ref1}(s) - Z_o(s)\, i_{o1}(s) \tag{5}$$

Where $G_{cl}(s)$ the close loop is transfer function of the control system, and $Z_o(s)$ is the output impedance.

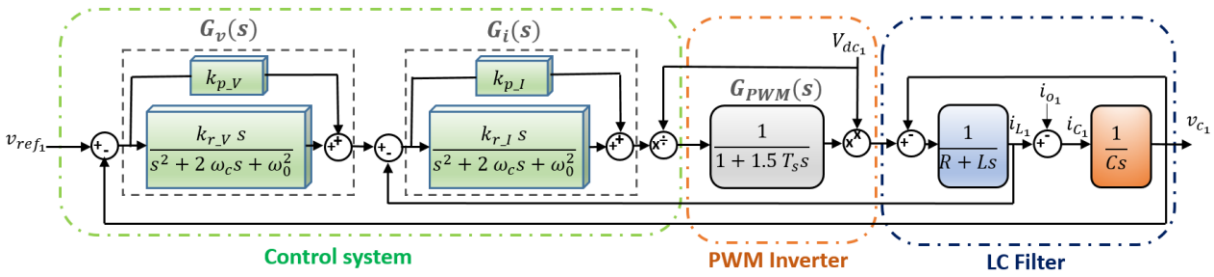

Fig 5. Block diagram of the inner control loops.

Figure (6) shows the Bode diagram of the closed-loop transfer function $G_{cl}(s)$, which represents how well the output voltage $v_{c1}(s)$ follows the reference voltage $v_{ref1}(s)$. Unity gain (0dB) around 50 Hz

indicate good tracking performance based on the system parameters given in Table (1). Additionally, Fig. (7) shows the Bode diagram of the output impedance $Z_o(s)$, which represents how much the output voltage is affected by load current $i_{o1}(s)$. A lower magnitude in $Z_o(s)$, especially around 50 Hz, indicates better disturbance rejection and improved voltage regulation under load changes. Around 608 Hz, there is a clear impedance peak of +28 dB. This comes from the closed-loop dynamics of the LC filter and the controllers. This kind of peak is typical in voltage‑controlled inverters. It means that without some form of damping, either active feedback or passive resistors (Xu & Xie, 2018), the system becomes more sensitive at those higher frequencies, where harmonics can excite the resonance.

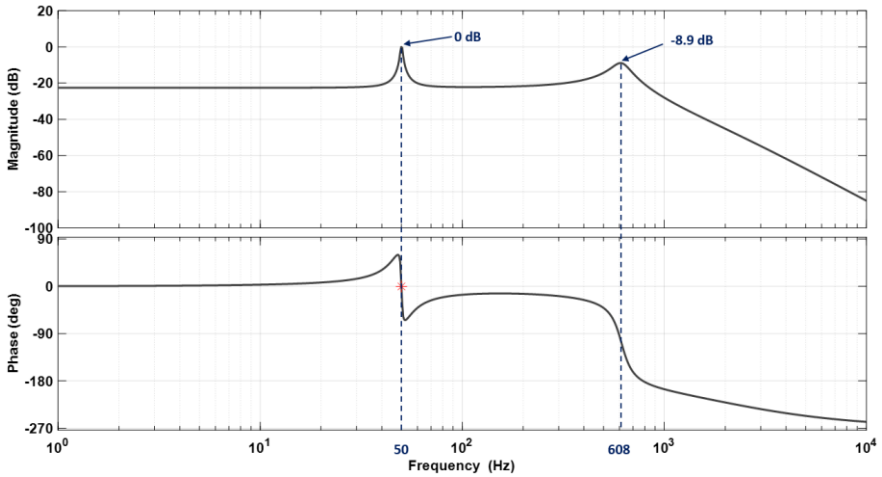

Fig 6. Bode diagram of the closed-loop transfer function of the inner control.

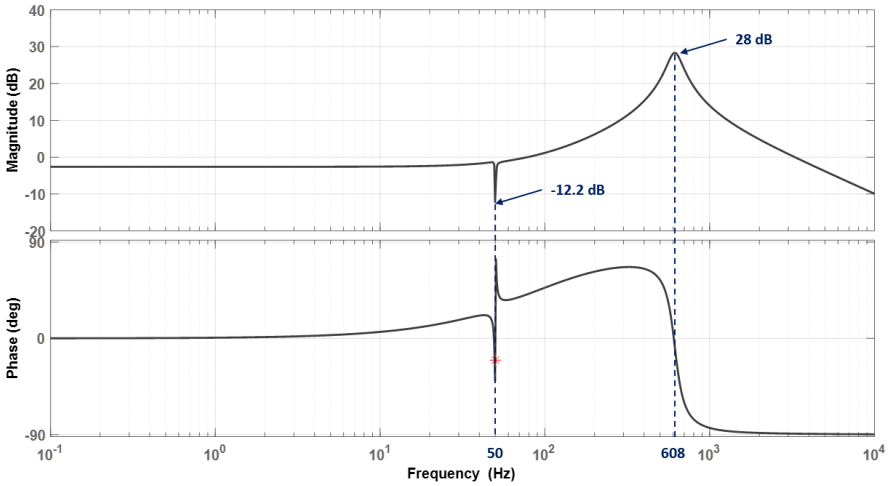

Fig 7. Bode diagram of the output impedance transfer function.

To analyze the stability of the inner control, the open-loop transfer function of the inner control is derived as follows:

$$G_{OL_{inner}}(s) = G_v(s)G_i(s)G_{PWM}(s)G_{LC}(s) \tag{6}$$

With:

$$G_{LC}(s) = \frac{1}{LC\,s^2 + RC\,s + 1} \tag{7}$$

The Bode diagram of the open-loop transfer function is depicted in Fig. (8). The analysis shows a phase margin of 84.3° at 50.7 Hz and a gain margin of 12.55 dB at 664.3 Hz, which are well above the recommended design lower limits of 30° for phase margin and 6 dB for gain margin. It should be noted that in the design, the internal resistance of the inductor, which in our case is equal to 0.5 Ohm, must be considered because it plays an important role in damping the system at the LC filter resonance frequency around 580 Hz. If not sufficient, other passive or active damping techniques can be applied. At 50 Hz, the open-loop transfer function exhibits a high gain of 29.1 dB, which is expected when using a PR controller. In our application, this gain is acceptable; however, in some applications with noise around 50 Hz, the gain may need to be reduced by adjusting the parameters of the non-ideal PR controller, such as increasing its bandwidth or reducing the proportional and resonant gains (Yao et al., 2017).

Table 1. AC microgrid setup parameters

	Symbol	Value	Description
Power stage	L_1	1.5 mH	Inverter-side filter inductor
	C	50 μF	Filter capacitor
	R_{l_1}, L_{l_1}	0.5Ω ,1 mH	Feeder line impedance for DG1
	R_{l_2}, L_{l_2}	0.5Ω ,0.5 mH	Feeder line impedance for DG2
	C_{DC}	2000 μF	DC link Capacitor of the inverter
	V_{DC}	40 V	Nominal DC link Voltage
	V_o	22 Vrms	Output voltage set point
	f_o	50 Hz	Frequency set point
	f_s	20 kHz	Sampling frequency
	f_{sw}	10 kHz	Switching frequency
Primary Control	k_{p_I}	1.2	Proportional gain of current PR controller
	k_{r_I}	0.5	Resonant gain of current PR controller
	k_{p_V}	0.12	Proportional gain of voltage PR controller
	k_{r_V}	0.5	Resonant gain of current PR controller
	L_v	3 mH	Nominal value of the virtual inductance
	m	0.03 rad/s/W	Frequency drooping gain
	n	0.01V/VAR	Voltage drooping gain
Synchronization			
	K_{SOGI}	0.7	SOGI damping factor
	γ	0.4	FLL integral gain
	K_{p_sync}	0.0001	PLL proportional gain of the PI
	K_{i_sync}	0.0006	PLL integral gain of the PI
Secondary Control			
	$k_{p\omega_sec}$	0.0001	Frequency proportional gain
	$k_{I\omega_sec}$	2	Frequency integral gain
	k_{pE_sec}	0.0002	Voltage amplitude proportional gain
	k_{IE_sec}	2	Voltage amplitude integral gain
	k_{pQ_sec}	0.0005	Reactive power compensation proportional gain
	k_{IQ_sec}	0.015	Reactive power compensation integral gain
	t_d	5ms	Delay of the low bandwidth communication

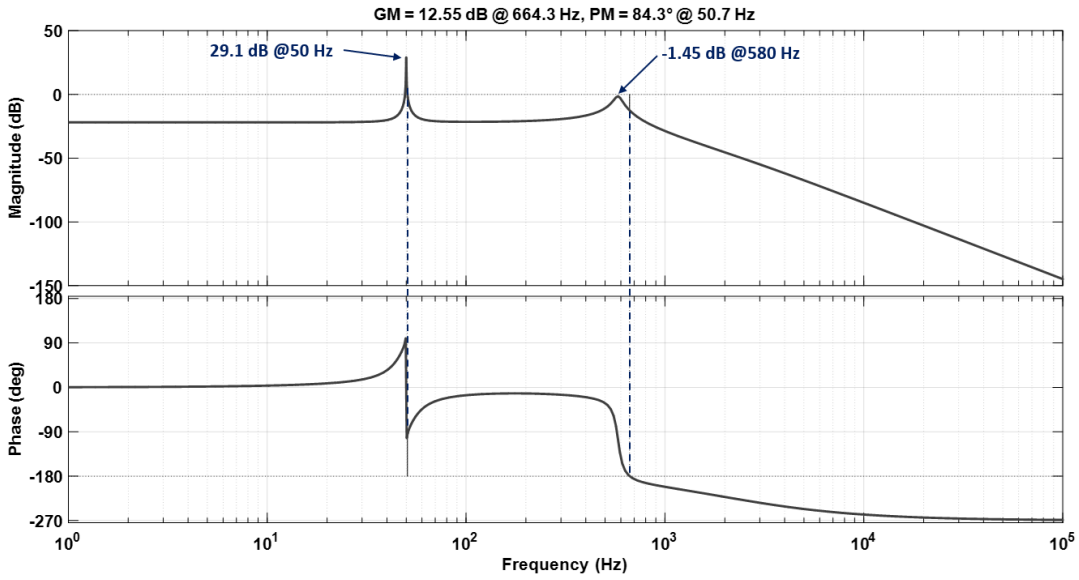

Fig 8. Bode diagram of the Inner control open-loop.

3.2 Synchronization Process

The synchronization procedure begins by connecting one inverter to form the microgrid. Then, the second inverter is operated without connecting it to the microgrid. During this phase, the synchronization process is enabled, which involves adding the appropriate phase angle to the second inverter using a Second-Order Generalized Integrator SOGI-based PLL enhanced with a Frequency-Locked Loop (FLL), also known as the SOGI-FLL PLL (Rodríguez et al., 2012), as shown in Fig. (9). The synchronization is based on the stationary reference frame (Han et al., 2016). The measured voltage at the point of common coupling v_{pcc} is passed through the SOGI block to generate output signals. This block removes noise and produces two outputs: one in phase with the input and the other in quadrature in the stationary reference frame (α, β). The output voltage signals and the closed-loop transfer functions can be written as follows:

$$\overrightarrow{v`_{pcc}} = \begin{pmatrix} v`_{pcc_\alpha} \\ v`_{pcc_\beta} \end{pmatrix}_{\alpha,\beta} \tag{8}$$

$$D(s) = \frac{V`_{pcc_\alpha}(s)}{V_{pcc}(s)} = \frac{k_{SOGI}\, \omega` s}{s^2 + k_{SOGI}\omega` s + \omega`^2} \tag{9}$$

$$Q(s) = \frac{V`_{pcc_\beta}(s)}{V_{pcc}(s)} = \frac{k_{SOGI}\, \omega`^2}{s^2 + k_{SOGI}\, \omega` s + \omega`^2} \tag{10}$$

Where $v`_{pcc}$ is the filtred version $v_{pcc}$, $k_{SOGI}$ is the damping factor of the SOGI, and $\omega`$ is the resonance frequency, which sould be adapted to the input signal frequency. This is realized using the FLL, which uses the frequency error defined as:

$$\varepsilon_f = \left(v_{pcc} - v`_{pcc_\alpha}\right) v`_{pcc_\beta} \tag{11}$$

It is shown in (Rodríguez et al., 2011) that the average of this frequency error is positive when $\omega < \omega`$, negative when $\omega > \omega`$, and zero when $\omega = \omega`$. This is why this error is passed through the integral gain γ with a negative sign, to drive the input toward zero based on the following equation:

$$\frac{d\omega`}{dt} = -\gamma\varepsilon_f \tag{12}$$

On the other hand, we can also choose v_{c2} to be the reference and write:

$$\overrightarrow{v_{c2}} = \begin{pmatrix} v_{c2} \\ 0 \end{pmatrix}_{\alpha,\beta} \tag{13}$$

We derive the amplitude of the vector product as follows:

$$\left\|\overrightarrow{v`_{pcc}} \text{ X } \overrightarrow{v_{c2}}\right\| = \left|v`_{pcc_\beta} * v_{c2}\right| \tag{14}$$

To synchronize v_{c2} with v_{pcc}, we aim to drive the amplitude of the vector product to zero. In this case, the average value of the amplitude of the vector product, calculated by the low pass filter, is passed through PI controller, which also serves as the virtual oscillator of the PLL and generates the phase angle added to v_{c2} until it becomes synchronized with v_{pcc}, as described in Fig. (9). The SOGI-FLL also determines the frequency and amplitude of the v_{pcc} signal. In our context, these values are known, and each inverter has the same nominal value at the start of the setup. Since no load is applied yet, v_{pcc} is the same as v_{c1}, which is why we focus solely on the phase.

Another important aspect often overlooked is the freezing block. After the synchronization process is completed and the second inverter is connected, the synchronization block must be stopped. This is because continuous synchronization is unnecessary, as a power angle, which is the phase angle difference between the inverter output voltage and v_{pcc}, is required to transfer power from the inverter to the PCC. However, stopping the synchronization block must be done while retaining the phase angle already added to v_{c2}; otherwise, its sudden removal could lead to an unwanted surge in power flow. The freezing block, depicted in Fig. (9), memorizes the phase angle and continues sending the same amount to v_{c2} even after the synchronization process is stopped. The synchronization parameters are shown in Table (1).

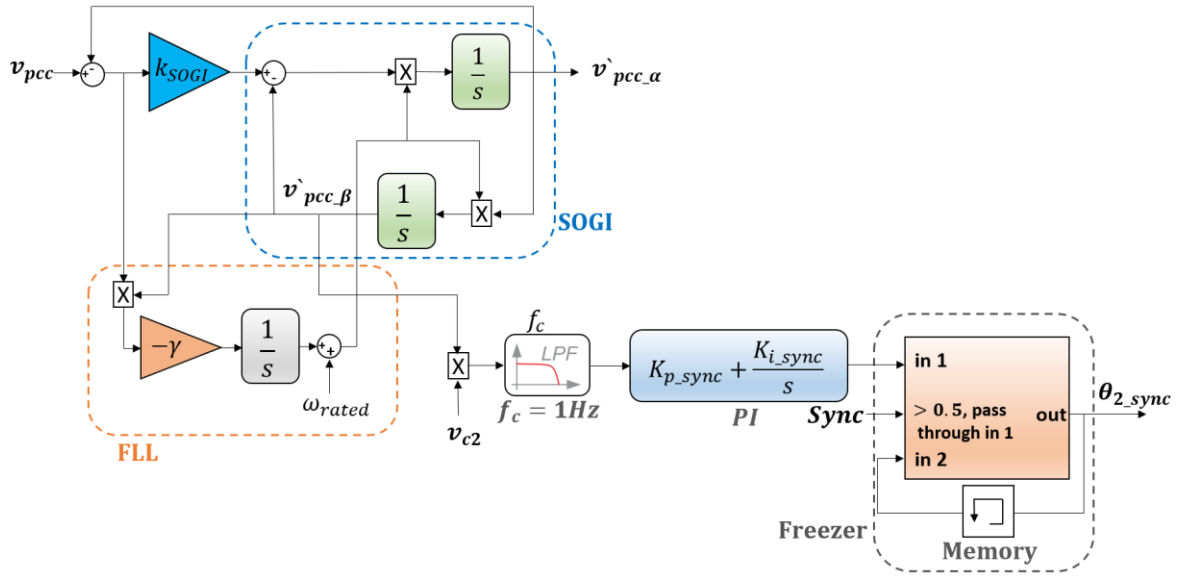

Fig 9. The synchronization process based on the SOGI-FLL PLL.

3.3 Droop Control

The droop-based load sharing method is a widely used approach for managing linear loads without the need for a centralized controller. In this method, each inverter-based distributed generator (DG) mimics the behavior of a conventional synchronous generator (Wang L. et al., 2023). It reduces its frequency when delivering more real power and lowers its voltage when supplying more reactive power. This strategy is commonly referred to as the conventional droop control (Guerrero et al., 2011). The frequency (ω) and voltage amplitude (V_p) of the reference signal can be defined as functions of the active and reactive power, respectively, as follows:

$$\omega = \omega^* - m\,P \tag{15}$$

$$V_p = V_p{}^* - n\,Q \tag{16}$$

Where ω^* and $V_p{}^*$represent the nominal frequency and peak voltage of the inverter output under no-load conditions. P and Q denote the fundamental active and reactive power delivered by the inverter, respectively. The parameters m and n are the droop coefficients, which define the sensitivity of the frequency and voltage adjustments in response to changes in the active and reactive power outputs. For each distributed generator i, m_i and n_i, are given by (de Souza et al., 2015):

$$m_i = \frac{\Delta\omega}{P_{i_{rated}}} \tag{17}$$

$$n_i = \frac{\Delta V}{Q_{i_{rated}}} \tag{18}$$

Where, $\Delta\omega$ and ΔV are the allowed angular frequency voltage magnitude deviations, respectively, and P_{i_rated} and Q_{i_rated} are the rated active and reactive powers of the DG_i, respectively.

For an islanded microgrid with two identical distributed generators DGs, Fig. (10). (a) shows the $P-\omega$ droop, where the slopes are identical. Since frequency is a global variable, the DGs experience the same frequency deviation, enabling them to share the same amount of active power. On the other hand, Fig. (10). (b) shows the $Q-V$ droop of the two DGs. Even though they have the same slope, the voltage deviation differs slightly due to line impedance mismatch. As voltage is a local variable that varies between DGs due to impedance mismatch, V_{PCC} is lower, resulting in an error in the steady state for reactive power sharing (Mohammed et al., 2023). Some designers ignore this issue, but in this paper, we address it further.

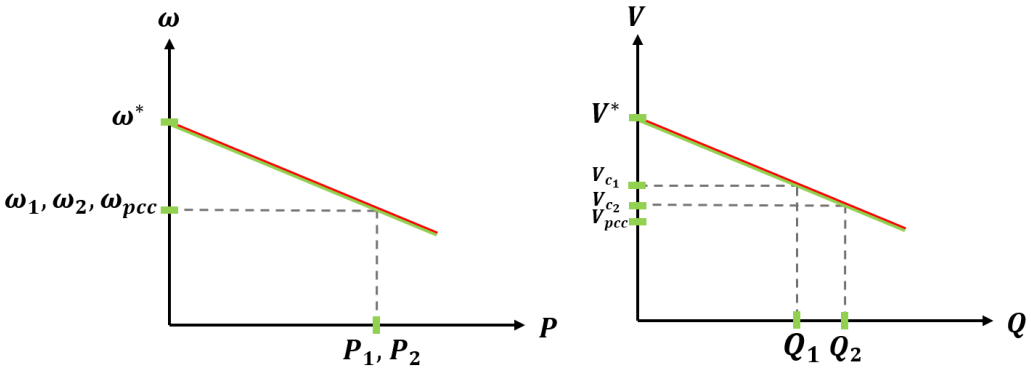

Fig 10. Active and reactive power sharing in an islanded ac microgrid with two DG, (a) $P-\omega$ Droop, (b) $Q-V$ Droop.

The power calculation procedure followed by the droop control is depicted in Fig. (11). Let us write $v_c(t) = V_c \cos(\omega t)$ and $i_o(t) = I_o \cos(\omega t - \varphi)$. The instantaneous power of this single-phase system can be expressed as follows:

$$p_{inst}(t) = v_c(t)\, i_o(t) \tag{19}$$

$$p_{inst}(t) = \frac{V_c\, I_o}{2}\cos(\varphi) + \frac{V_c\, I_o}{2}\cos(2\omega t - \varphi) \tag{20}$$

The term $\cos(2\omega t - \varphi)$ can be expanded to derive the instantaneous active power $p_1(t)$ and the instantaneous reactive power $q_1(t)$ as below:

$$\begin{cases} p(t) = \dfrac{V_c}{\sqrt{2}}\dfrac{I_o}{\sqrt{2}}\cos(\varphi)[1 + \cos(2\omega t)] \\ q(t) = \dfrac{V_c}{\sqrt{2}}\dfrac{I_o}{\sqrt{2}}\sin(\varphi)\sin(2\omega t) \end{cases} \tag{21}$$

From the previous development, we can see that passing the instantaneous power $p_{inst}(t)$ through a low-pass filter eliminates the fluctuating part, giving the average active power. To obtain the average reactive power, we apply a delay of a quarter-period of the fundamental frequency to the input voltage, resulting in $v_c` = V_c \sin(\omega t)$ (Yang & Blaabjerg, 2013) . The corresponding instantaneous power is then calculated as follows:

$$p`_{inst}(t) = v_c`(t)\, i_o(t) = p`(t) + q`(t) \tag{22}$$

Where:

$$\begin{cases} p`(t) = \dfrac{V_c}{\sqrt{2}}\dfrac{I_o}{\sqrt{2}}\cos(\varphi)\sin(2\omega t) \\ q`(t) = \dfrac{V_c}{\sqrt{2}}\dfrac{I_o}{\sqrt{2}}\sin(\varphi)[1 + \cos(2\omega t)] \end{cases} \tag{23}$$

By using a low-pass filter on the instantaneous power $p`_{inst}(t)$, we can obtain the average reactive power, which is used along with the average active power in the droop control to determine the angular frequency and voltage amplitude to be added to the voltage reference generator in the inner control loops. The reference voltage from the droop controller is expressed as:

$$v_{droop} = V_{Droop} \sin(\omega_{Droop}\, t) \tag{24}$$

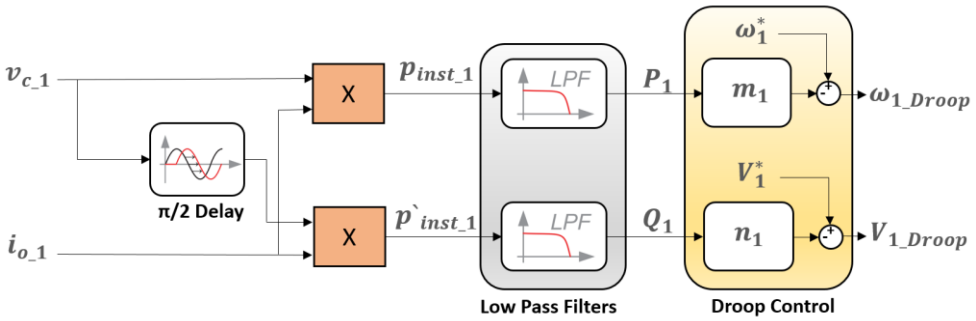

Fig 11. Power calculation and droop control for DG1.

3.4 Virtual Impedance

The aforementioned droop control equations are primarily valid for inductive networks, such as those found in high-voltage transmission systems. However, in low-voltage microgrids particularly in residential applications, the line impedance is predominantly resistive, as the reactance-to-resistance ratio (X/R) is typically much less than 1 (John et al., 2017). In such contexts, conventional droop control becomes less effective due to the stronger coupling between active and reactive power. To address this, virtual impedance control is employed to emulate an inductive impedance. This emulation helps decouple active and reactive power flows and mitigates the impact of line impedance on power sharing accuracy (Prasad & Parimi, 2023). Consequently, the droop controller's output reference voltage is modified to include the virtual impedance Z_v , resulting in an adjusted reference voltage v_{ref}, which can be expressed as follows:

$$v_{ref} = v_{droop} - Z_v \; i_o \tag{25}$$

The implementation of the virtual impedance block is detailed in Fig. (12), where the virtual resistance is multiplied by the input current. For the virtual inductor, a high-pass filter is used to implement the derivative action, with a cutoff frequency of $\omega_{c_HP} = 314\, rad/s$. This structure represents a derivative action in series with a low-pass filter to reduce high-frequency noise.

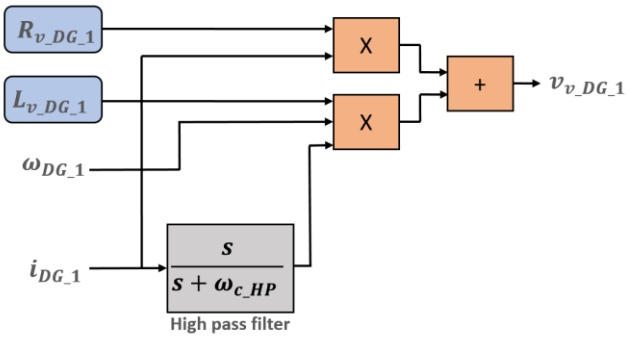

Fig 12. The virtual impedance block for DG1.

3.5 Secondary Control

To compensate for the steady-state errors introduced by the droop control, the secondary control system sends restoration reference signals, which are added to the reference voltage signal of each inverter (Guerrero et al., 2011; Khayat et al., 2020). These signals are based on the nominal values of frequency and voltage amplitude. In this case, a centralized secondary control architecture is implemented as shown in Fig. (13), where Proportional-Integral (PI) controllers are employed to ensure accurate voltage and frequency restoration (Esmaeili Karkevandi et al., 2018). The control mechanism can be expressed as follows:

$$\omega_{sec} = k_{p\omega s}(\omega^*_{MG} - \omega_{MG}) + k_{i\omega s} \int (\omega^*_{MG} - \omega_{MG})\, dt \tag{26}$$

$$E_{sec} = k_{pVs}(E^*_{MG} - E_{MG}) + k_{iVs} \int (E^*_{MG} - E_{MG})\, dt \tag{27}$$

Where, $k_{p\omega s}$, $k_{i\omega s}$, $k_{pVs}$and k_{iVs} are the control parameters of the secondary controller.

It should be noted that the references produced by the secondary controller, ω_{sec} and E_{sec}, must be limited to not exceed the allowed deviations. Fig. (13) shows the block diagram of the secondary control loops, used to design the PI controller parameters and analyze the stability of the system. Figure (13). (a) presents the frequency restoration loop, where the communication delay is modeled as a first-order lag represented by the transfer function $G_d(s)$ (Vasquez et al., 2013). The active power droop control loop is also included with its low-pass filter $G_{LPF}(s)$. A simple model representing the PLL loop is added to feature the frequency measurement effect. In this case, as the PLL bandwidth is much larger than that of the secondary control, a simple first-order delay is chosen, where τ is a constant representing how quickly the PLL responds, set to $\tau = 30ms$ in our study (Wang R. et al., 2023). Moreover, Fig. (13). (b) shows the block diagram of the voltage amplitude restoration loop, taking into account the communication delay, as explained previously, modeled by $G_d(s)$, and the reactive power droop control loop. The measurement of the voltage amplitude is considered a unity gain in this case. From the above diagrams, we can derive the following close-loop equations:

$$\omega_{MG} = \frac{G_{\omega_sec}(s)G_d(s)}{1 + G_{\omega_sec}(s)G_d(s)G_{PLL}(s)}\omega^*_{MG} - \frac{mG_{LPF}(s)}{1 + G_{\omega_sec}(s)G_d(s)G_{PLL}(s)}p_{inst} \quad (28)$$

$$E_{MG} = \frac{G_{E_sec}(s)G_d(s)}{1 + G_{E_sec}(s)G_d(s)}E^*_{MG} - \frac{nG_{LPF}(s)}{1 + G_{E_sec}(s)G_d(s)}p`_{inst} \quad (29)$$

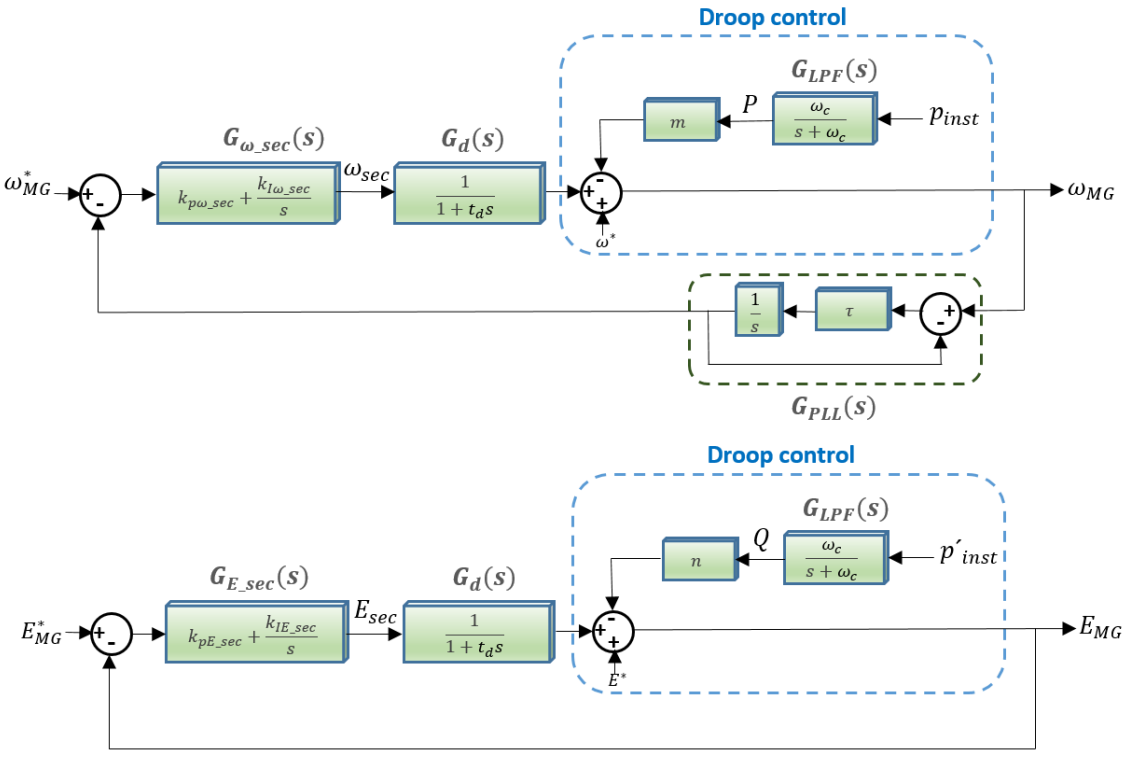

Fig 13. Block diagram of the secondary control loops, (a) frequency restoration, (b) Voltage amplitude restoration.

The step response of the system to a sudden change in the active power reference by 200 W at t=1s, is depicted in Fig. (14), where the $p_{inst} - to - \omega_{MG}$ transfer function is used, and the parameters of the secondary control detailed in Table 1 are considered. The system demonstrates good performance in handling this sudden change, smoothly restoring the frequency to the nominal value of 50 Hz with no

(a)

overshoot after approximately 3.5 seconds, which is accepted from the perspective of the secondary control response timescale.

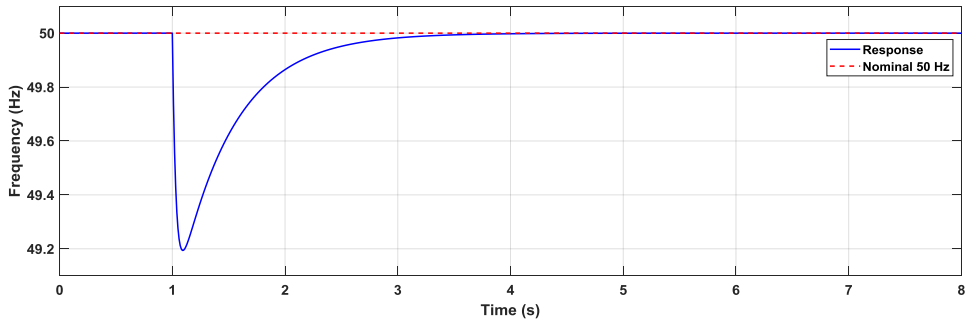

Fig 14. Step Response P-to- ω_{MG} : 200 W Disturbance at t=1 s with 5 ms communication delay.

Figure (15) shows the Bode diagram of the closed-loop transfer function of the frequency restoration secondary control. At low frequencies, the gain is 0 dB, which means the reference is tracked without amplification. The bandwidth of the controller is estimated at -3 dB to be 0.35 Hz, which is within the standards for islanded AC microgrids, as it ensures that the secondary controller does not interact with the inner controller.

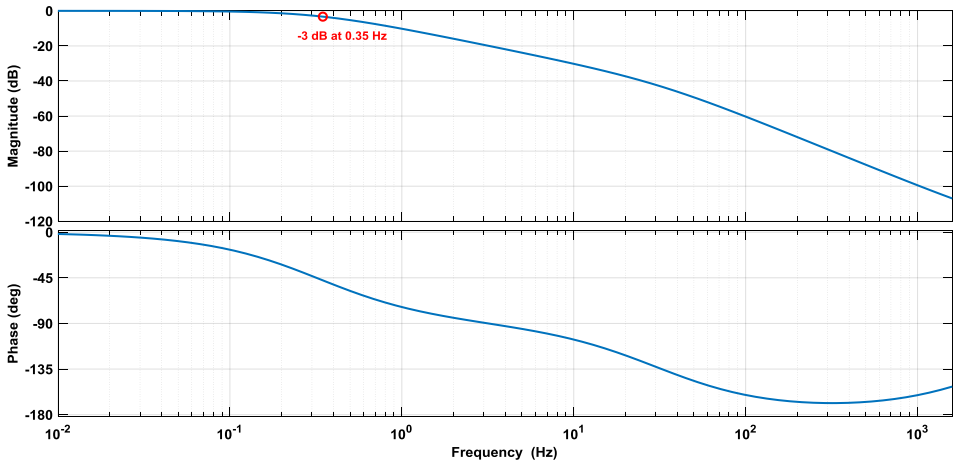

Fig 15. Bode diagram for the Close-Loop transfer function $\omega^{*}_{MG} - to - \omega_{MG}$.

Moreover, to analyze the stability of the system, the Bode diagram of the open-loop frequency restoration control is presented in Fig. (16). It shows a gain margin of 45.9 dB at 31.2 Hz and a phase margin of 88.8° at 0.318 Hz, demonstrating the stability of the control system. However, the gain margin indicates an overdamped system, as the recommendation for a safe zone is a gain margin greater than 6 dB. Reducing the PI controller gains is the usual procedure to lower the gain margin, but this would increase the bandwidth, which should be avoided for the secondary control.

Figure (17) depicts the step response of the transfer function for a sudden change of 100 VAR in the reactive power. The secondary control demonstrates good capability to restore the voltage magnitude of the microgrid to the nominal value of 22 V in a smooth manner after 4 seconds. At the same time, the closed-loop Bode diagram in Fig. (18) shows unity gain at low frequencies and a bandwidth of 0.35 Hz at -3 dB, which is what the designer of the secondary control aims for, as explained previously. The stability of the voltage amplitude restoration secondary controller is also analyzed using the Bode

diagram of the open-loop transfer function presented in Fig. (19), which shows an infinite gain margin and a phase margin of 89.4°. As explained previously, the objective is not only to optimize the controller characteristics but also to maintain the bandwidth of the secondary controller far from the inner control loops to eliminate any interaction.

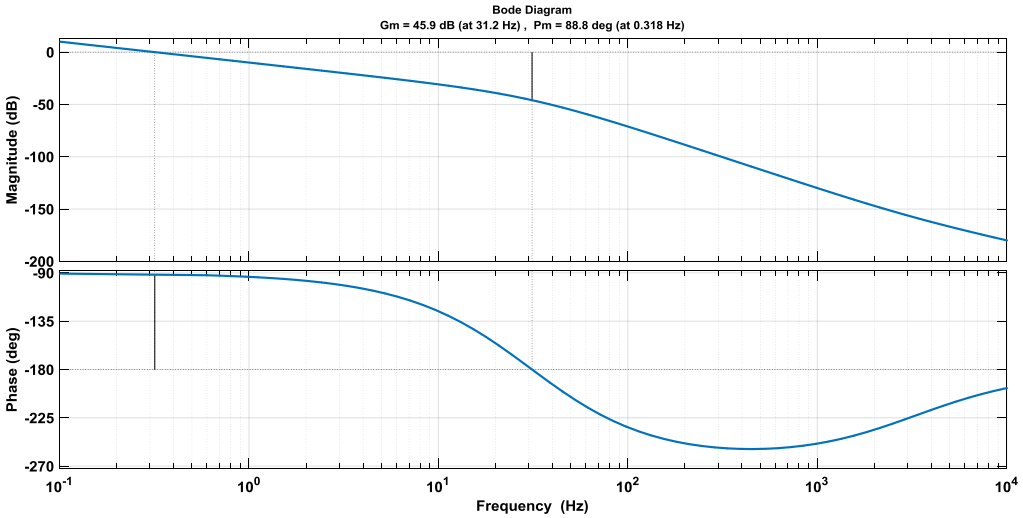

Fig 16. Open-Loop Bode Diagram for the frequency restoration.

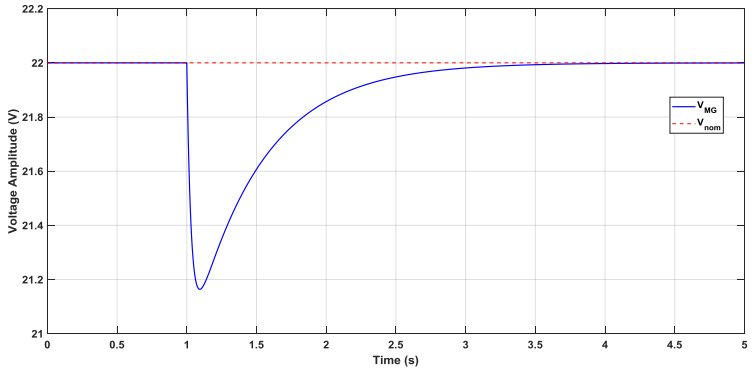

Fig 17. Step Response: 100 VAR Disturbance at t=1 s with 5 ms communication delay.

Reactive power sharing between inverters remains challenging even when advanced droop control techniques are employed. This difficulty primarily arises from line impedance effects that cause voltage variations at different points in the network (Micallef et al., 2014). Since reactive power distribution largely depends on voltage amplitudes, achieving a balanced share among generators is inherently complex. To address this, we implemented a centralized secondary control strategy that sends reference commands to both inverters, ensuring that reactive power is distributed proportionally to their nominal capacities, the dedicated centralized secondary controller is applied as follows:

$$V_{qsec1} = k_{pQs}(Q_m - Q_1) + k_{iQs} \int (Q_m - Q_1)\, dt \tag{30}$$

$$V_{qsec2} = k_{pQs}(Q_m - Q_2) + k_{iQs} \int (Q_m - Q_2)\, dt \tag{31}$$

Where, Q_m, the mean value of the reactive power, in the case of two DGs we have:

$$Q_m = \frac{Q_1 + Q_2}{2} \tag{32}$$

This consensus algorithm ensures convergence, allowing each generator to share the appropriate amount of reactive power and eliminate the steady-state error introduced by the droop control (Khayat et al., 2020; Wu et al., 2014).

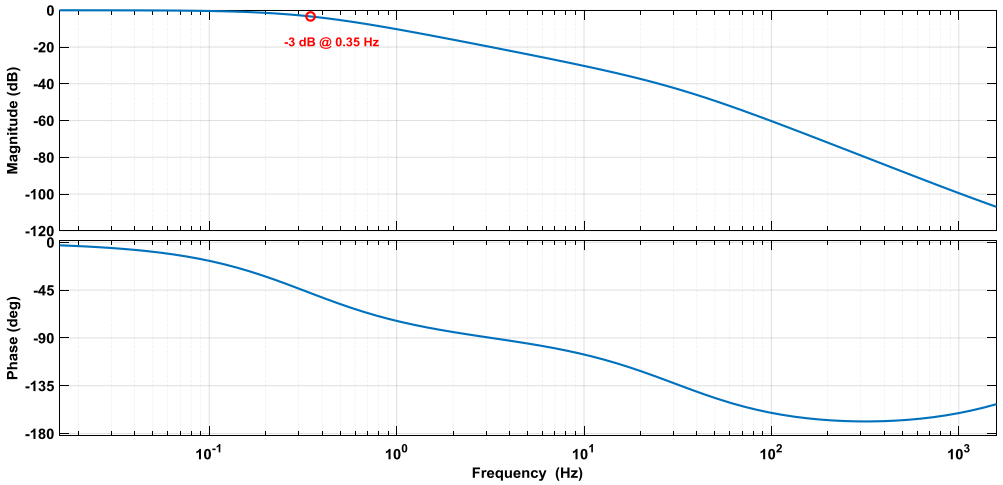

Fig 18. Bode diagram for the Close-Loop transfer function $E^*_{MG} - to - E_{MG}$.

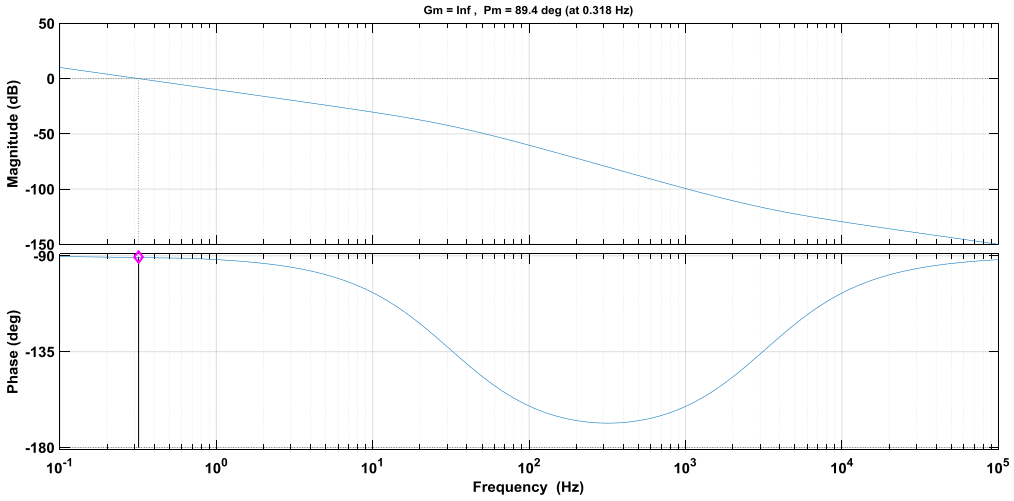

Fig 19. Open-Loop Bode Diagram for the voltage amplitude restoration.

4. EXPERIMENTAL RESULTS

Figure (20) shows the experimental setup, which uses SEMIKRON SEMITEACH IGBT-based inverters, selected for their robustness and suitability for research applications. Each inverter provides individual gate access to each IGBT driver through BNC connectors. The PWM signals are generated by STM32F4 Discovery microcontroller boards, chosen for their reliability, low cost, and easy integration with Simulink via the Waijung Toolbox. These boards receive the duty-cycle references computed by the dSPACE 1103 platform and generate the corresponding PWM signals. 4N25

optocouplers ensure galvanic isolation between the control and power stages and boost the PWM voltage from 3.3 V to 15 V. These components are well known, low cost, and widely available, making them a good choice for reproducible research setups. A closer view of the LEM current and voltage measurement cards, together with the STM32F4 board and isolation interface, is shown in Fig. (21). Table (1) summarizes the main parameters of the setup.

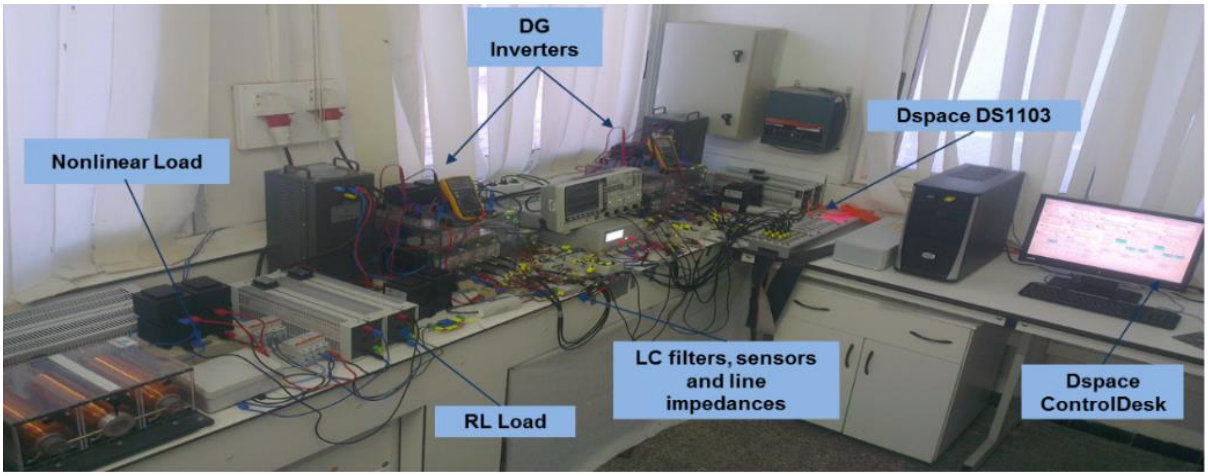

Fig 20. Experimental setup of the islanded AC microgrid.

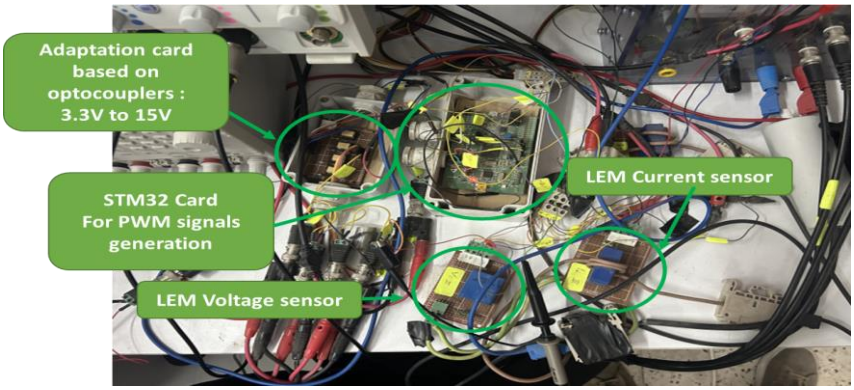

Fig 21. Measurements and PWM signals generation.

Figure (22) shows the interactive interface for the experimental test bench, developed using dSPACE ControlDesk. This platform allows real-time visualization of electrical parameters (voltages and currents), total harmonic distortion (THD) levels of voltages, active and reactive power generation, and control parameters, activating the synchronization process, droop control, and secondary control with reactive power compensation, all of which can be adjusted in real time. Figure (23) displays the three output voltages measured at the capacitors of the LC filters of the distributed generators, as well as at the common bus, where the apparent difference in amplitude is due to variations in the measurement gains of the LEM LV 25-P sensors. The PCC voltage is particularly significant in power quality studies, as it determines the voltage supplied to newly connected loads within the microgrid. To illustrate this concept, a test with a non-linear load, realized using a diode bridge feeding an RC circuit, is performed.

Figure (24) shows the output voltages and the v_{PCC} voltage in the presence of a non-linear load, revealing that the voltage quality at the PCC, with a THD of 7.42%, is more affected than the inverter output voltages (THD_v_{c1} = 2.97% and THD_v_{c2} = 3.29%). This is due to the harmonic voltage drop in the feeder line impedances caused by the non-linear current, which worsens the v_{PCC} quality. Additionally, the difference in voltage quality between the inverters is attributed to the absence of harmonic

compensation control; since the developed inner control and power sharing address only the fundamental frequency, the harmonic current, as shown in Fig. (25), flows through the path with less impedance. Given the line impedances Z_{line_1} (R_{l_1} = 0.5 Ω, L_{l_1} = 1 mH) and Z_{line_2} (R_{l_2}= 0.5 Ω, L_{l_2} = 0.5 mH), more harmonic current passes through Z_line2, leading to a greater harmonic voltage drop across the output impedance of distributed generator 2, resulting in higher distortion (THD_v_{c2} = 3.29%). This indicates that an appropriate harmonic compensation strategy is needed to reduce distortion and ensure proper harmonic current sharing.

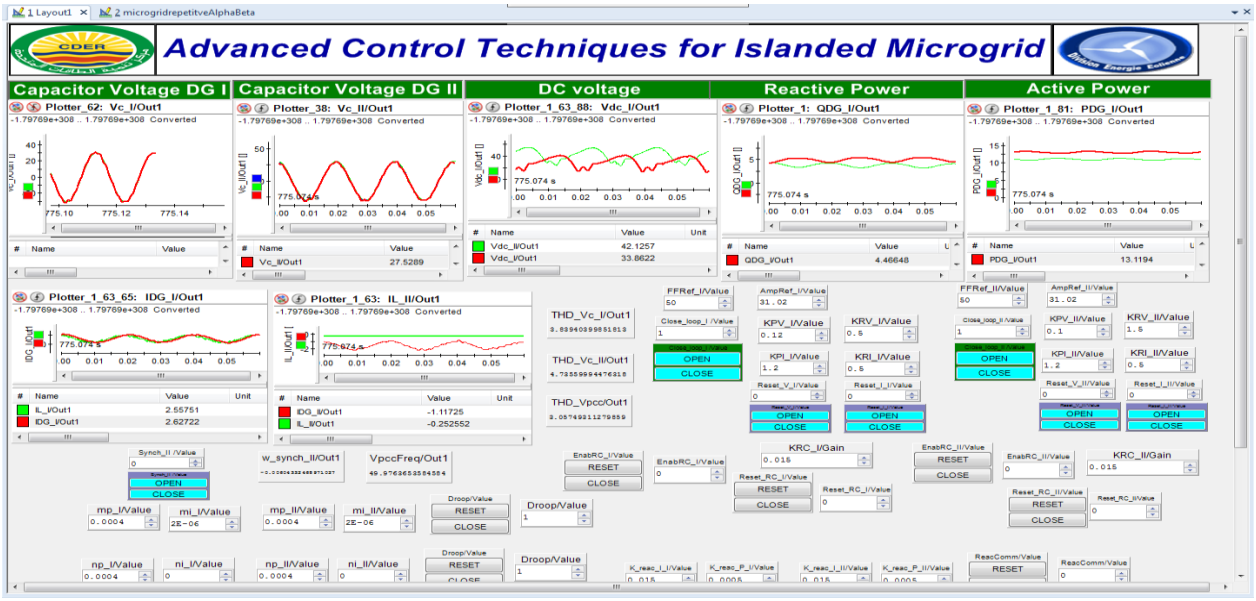

Fig 22. Interactive platform developed using dSPACE-ControlDesk for the microgrid test bench.

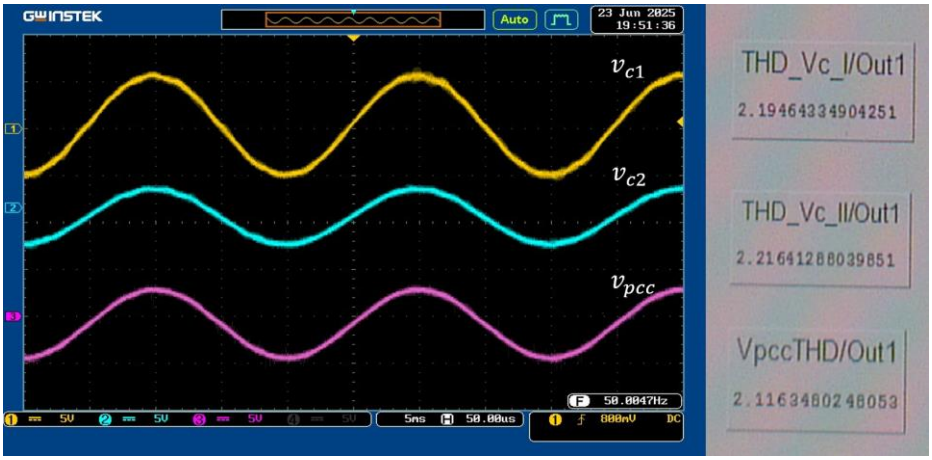

Fig 23. Output voltages at the DGs and PCC with a linear load.

The synchronization of the generation units was achieved using a SOGI-FLL PLL technique, known for its robustness against disturbances, as illustrated in Fig. (26), which shows the synchronization process between the DG2 generator and the PCC bus. The process starts at 788.02 s experimental time, as depicted in the leftmost plot of Fig. (26), and concluding around 796.27 s, taking approximately 8 s, which is acceptable from an experimental perspective. The freezing block ensures that the voltage remains synchronized even after stopping the synchronization process. After connecting DG2 to the microgrid, we disable the synchronization and enable droop control by clicking on a specific button in the interactive interface, and we connect after a linear load consisting of a variable resistance of 33 Ω in series with an inductor of 18 mH. The performance of the droop control is shown in Fig. (27), where

equitable active power sharing is achieved between the two distributed generators (DGs) without communication, relying solely on frequency as a global variable. However, for reactive power sharing, droop control alone cannot achieve equitable sharing, reducing the reactive power difference but leaving a steady-state error, as shown in Fig. (27), due to impedance mismatches and the fact that voltage is not a global variable in the microgrid. To address this, a reactive power compensation technique is implemented at the secondary control level; after enabling this control via the interactive interface, the steady-state error is eliminated, as shown in Fig. (28), where both active and reactive power are equitably shared between the DGs.

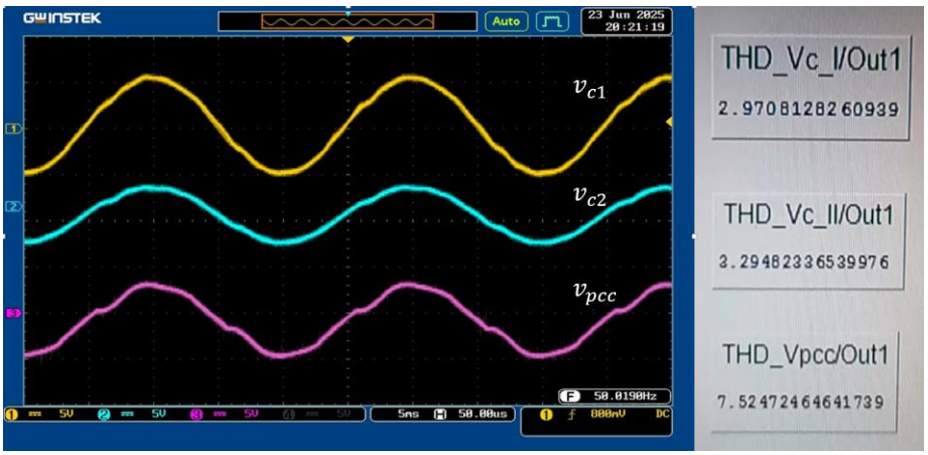

Fig 24. Output voltages at the DGs and PCC with a non-linear load.

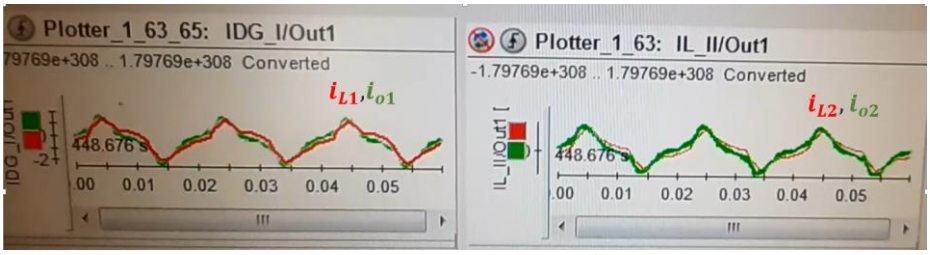

Fig 25. Inductor and output currents of the DGs with a nonlinear load.

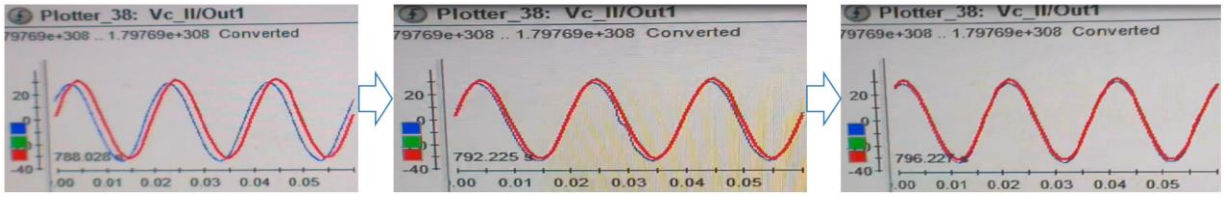

Fig 26. Synchronization process using the SOGI-FLL PLL technique.

The performance of the secondary control for frequency and voltage restoration in the microgrid is presented in Fig. 29. Figure (29) (a) shows the system without secondary control, with a v_{PCC} voltage magnitude of 21.16 V and a frequency of 49.91 Hz. After enabling the secondary controller, the results are depicted in Fig. (29)(b). The voltage magnitude at the PCC reaches 21.76 V, the output of the first inverter (DG1) reaches 22.07 V, and the output of the second inverter (DG2) reaches 22.11 V, while the microgrid frequency is restored to 50 Hz. This demonstrates the effectiveness of the secondary control in restoring both the frequency and voltage amplitude to their nominal values, with some acceptable errors in voltage amplitudes.

Fig 27. Power sharing using only the droop control.

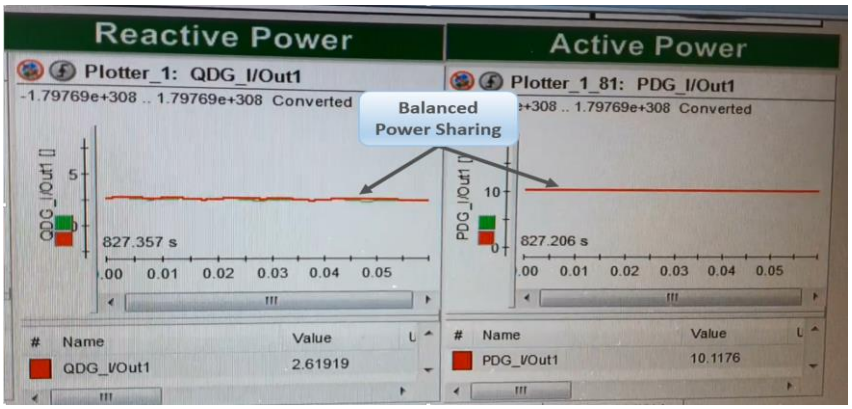

Fig 28. Power sharing using droop control and reactive power compensation.

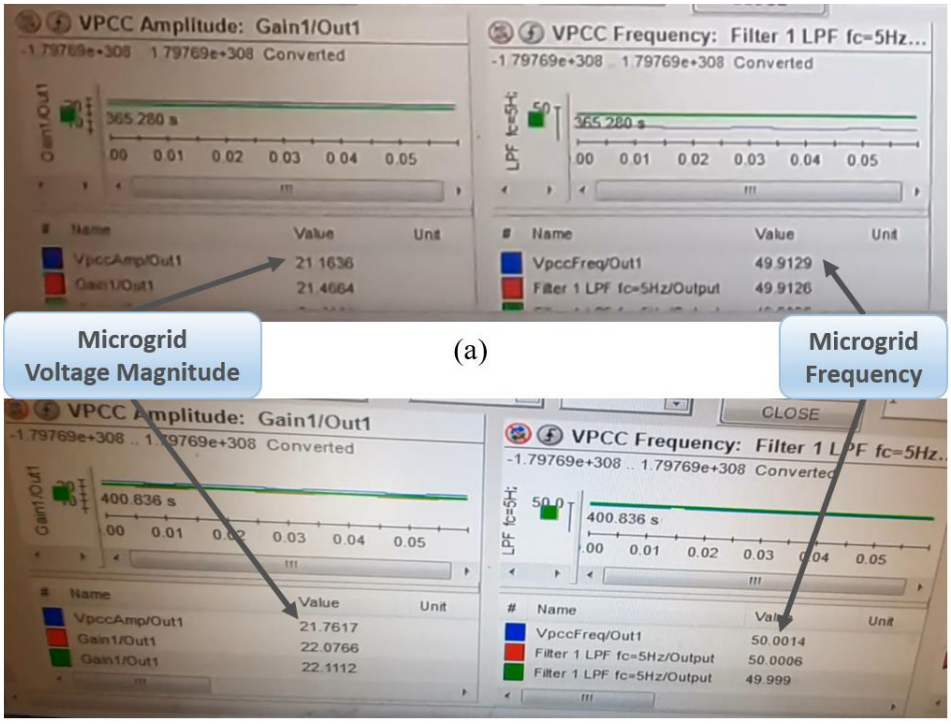

Fig 29. Secondary control performance for voltage amplitude and frequency restoration.

5. CONCLUSION

Moving toward a more electrical and sustainable future, integrating more renewable energy into power systems is inevitable. However, renewables like solar and wind, at high penetration levels, cause instability in traditional power grids due to their variable nature. Microgrids offer a solution by locally managing renewable sources and coordinating energy production and demand intelligently. They reduce losses in transmission lines and support the main grid with auxiliary services like black start, voltage regulation, reactive power compensation, and power quality improvement. Despite the importance of this subject, building test beds for research and education is tough because existing solutions are complex, expensive, and not scalable. Our goal was to create a practical, affordable tool for researchers and students to learn and experiment with AC microgrid control by developing and validating a single-phase islanded AC microgrid setup. We aimed to explain core control concepts to help students and researchers understand and build on microgrid technology.

The microgrid uses two distributed generators (inverters) feeding linear and nonlinear loads. The design is modular and cost-effective, using STM32F4 Discovery boards to generate PWM signals, reducing the computational load on the dSPACE system. A dSPACE1103 was enough to handle all calculations and implement the full hierarchical control strategy, which includes inner loop Proportional-Resonant controllers for voltage regulation, Phase-Locked Loop synchronization based on Second-Order Generalized Integrator with Frequency-Locked Loop (SOGI-FLL), virtual impedance for decoupling active and reactive powers, especially important in resistive low-voltage systems, droop control for power sharing, and a secondary controller for voltage amplitude, frequency restoration, and reactive power compensation.

Experimental results show the system maintains stable voltage, synchronizes inverters at the point of common coupling, shares load effectively between inverters, and restores microgrid voltage and frequency to nominal values under various load conditions. Looking ahead, as harmonic control is an important auxiliary control, we plan to improve voltage quality at the primary control level and coordinate the harmonic compensation effort between the DGs. It is also known that distributed secondary control is more robust than the centralized one, as the latter has a single point of failure. We will consider using distributed consensus schemes at the secondary level. The realized setup can also be optimized by applying advanced methods like predictive control, adaptive droop control, and energy storage integration. Furthermore, integrating the complete renewable energy system, including source dynamics with different penetration levels, would provide a more comprehensive experimental platform for studying the interaction between renewable sources and microgrid control.

REFERENCES

Buraimoh, E., Aluko, A. O., Oni, O. E., & Davidson, I. E. (2022). Decentralized virtual impedance–conventional droop control for power sharing for inverter-based distributed energy resources of a microgrid. Energies, 15(12), 4439. DOI: 10.3390/en15124439.

Chakraborty, S., Wang, J., Ganguly, S., & Kroposki, B. (2024). Development of a practical secondary control for hardware microgrids. IEEE Energy Conversion Congress and Exposition (ECCE), Phoenix, AZ. DOI: 10.1109/ECCE55643.2024.10860894.

Daneshvar, M. R., Asadi, S., & Mohammadi‐Ivatloo, B. (2021). Grid Modernization – Future Energy Network Infrastructure: Overview, Uncertainties, Modelling, Optimization, and Analysis. Power Systems series. Cham, Switzerland: Springer. ISBN 978‐3‐030‐64098‐9. DOI: 10.1007/978‐3‐030‐64099‐6.

de Souza, W. F., Severo Mendes, M. A., & Lopes, L. A. C. (2015). Power sharing control strategies for a three-phase microgrid in different operating conditions with droop control and damping factor investigation. IET Renewable Power Generation, 9(7), 831–839. DOI: 10.1049/iet-rpg.2014.0250.

Esmaeili Karkevandi, A., Daryani, M. J., & Usta, O. (2018). ANFIS-Based Intelligent PI Controller for Secondary Frequency and Voltage Control of Microgrid. 2018 IEEE PES Innovative Smart Grid Technologies Conference Europe (ISGT-Europe), Sarajevo, Bosnia and Herzegovina. DOI: 10.1109/ISGTEurope.2018.8571748.

Ferrari, M., Starke, M., Smith, J., Ollis, B., Sundararajan, A., & Garcia, Y. (2024). A Networked Microgrid Framework and Testbed for Communication, Controls, and Optimization Testing. 2024 IEEE Energy Conversion Congress and Exposition (ECCE), Phoenix, AZ, USA. DOI: 10.1109/ECCE55643.2024.10860879.

Govind, D., Suryawanshi, H. M., Nachankar, P., Narayana, C. L., & Singhal, A. (2023). A modified voltage controller with advanced droop control for load sharing in standalone AC microgrid under different load conditions. IEEE Transactions on Industry Applications, 59(5), 5818–5831. DOI: 10.1109/TIA.2023.3290931.

Guerrero, J. M., Vasquez, J. C., Matas, J., de Vicuna, L. G., & Castilla, M. (2011). Hierarchical control of droop-controlled AC and DC microgrids—A general approach toward standardization. IEEE Transactions on Industrial Electronics, 58(1), 158–172. DOI: 10.1109/TIE.2010.2066534.

Haidekker, M. A., Liu, M., & Song, W. (2023). Alternating-current microgrid testbed built with low-cost modular hardware. Sensors, 23(6), 3235. DOI: 10.3390/s23063235.

Han, Y., Luo, M., Zhao, X., Guerrero, J. M., & Xu, L. (2016). Comparative Performance Evaluation of Orthogonal-Signal-Generators-Based Single-Phase PLL Algorithms—A Survey. IEEE Transactions on Power Electronics, 31(5), 3932–3944. DOI:10.1109/TPEL.2015.2466631.

He, J. J., Van Bossuyt, D. L., & Pollman, A. (2022). Experimental validation of systems engineering resilience models for islanded microgrids. Systems, 10(6), 245. DOI: 10.3390/systems10060245.

Hirsch, A., Parag, Y., & Guerrero, J. M. (2018). Microgrids: A review of technologies, key drivers, and outstanding issues. Renewable and Sustainable Energy Reviews, 90, 402–411. DOI: 10.1016/j.rser.2018.03.040.

John, B., Ghosh, A., & Zare, F. (2017). Droop control in low voltage islanded microgrids for sharing nonlinear and unbalanced loads. 2017 IEEE Region 10 Symposium (TENSYMP), Cochin, India. DOI: 10.1109/TENCONSpring.2017.8069980.

Khayat, Y., Shafiee, Q., Heydari, R., Naderi, M., Dragicevic, T., Simpson-Porco, J. W., Dörfler, F., Fathi, M., Blaabjerg, F., Guerrero, J. M., & Bevrani, H. (2020). On the secondary control architectures of AC microgrids: An overview. IEEE Transactions on Power Electronics, 35(6), 6482–6500, DOI:10.1109/TPEL.2019.2951694.

Lian, Z., Wen, C., Guo, F., Lin, P., & Wu, Q. (2023). Decentralized secondary control for frequency restoration and power allocation in islanded AC microgrids. International Journal of Electrical Power & Energy Systems, 148. DOI: 10.1016/j.ijepes.2022.108927.

Lidula, N. W. A., & Rajapakse, A. D. (2011). Microgrids research: A review of experimental microgrids and test systems. Renewable and Sustainable Energy Reviews, 15(1), 186–202. DOI: 10.1016/j.rser.2010.09.041.

Micallef, A., Apap, M., Spiteri Staines, C., Guerrero, J. M., & Vasquez, J. C. (2014). Reactive power sharing and voltage harmonic distortion compensation of droop controlled single phase islanded microgrids. IEEE Transactions on Smart Grid, 5(3), 1149–1158. DOI: 10.1109/TSG.2013.2291912.

Mohammed, N., Lashab, A., Ciobotaru, M., & Guerrero, J. M. (2023). Accurate reactive power sharing strategy for droop-based islanded AC microgrids. IEEE Transactions on Industrial Electronics, 70(3), 2696–2707. DOI: 10.1109/TIE.2022.3167141.

Prasad, P. S., & Parimi, A. M. (2023). Design and analysis of decentralized virtual impedance based controller for enhancing power sharing and stability in an islanded microgrid. Journal of Electrical Engineering & Technology, 18(2), 1769–1783. DOI: 10.1007/s42835‑022‑01336‑4.

Quizhpe, K., Arévalo, P., Ochoa-Correa, D., & Villa-Ávila, E. (2024). Optimizing microgrid planning for renewable integration in power systems: A comprehensive review. Electronics, 13(18). 3620. DOI : 10.3390/electronics13183620.

Rodríguez, P., Luna, Á., Candela, I., Mujal‑Rosas, R., Teodorescu, R., Blaabjerg, F. (2011). Multiresonant frequency-locked loop for grid synchronization of power converters under distorted grid conditions. IEEE Transactions on Industrial Electronics, 58(1), 127–138. DOI: 10.1109/TIE.2010.2042420.

Rodríguez, P., Luna, A., Muñoz-Aguilar, R. S., Etxeberria-Otadui, I., Teodorescu, R., & Blaabjerg, F. (2012). A Stationary Reference Frame Grid Synchronization System for Three-Phase Grid-Connected Power Converters Under Adverse Grid Conditions. IEEE Transactions on Power Electronics, 27(1), 99–112. DOI: 10.1109/TPEL.2011.2159242.

Rodriguez-Martinez, O. F., Andrade, F., Vega Penagos, C. A., & Luna, A. C. (2023). A review of distributed secondary control architectures in islanded inverter-based microgrids. Energies, 16(2), 878. DOI: 10.3390/en16020878.

Shrivastava, S., & Subudhi, B. (2020). Comprehensive review on hierarchical control of cyber-physical microgrid system. IET Generation, Transmission & Distribution, 14(26), 6397–6416. doi:10.1049/iet-gtd.2020.0464. DOI: 10.1049/iet-gtd.2020.0971.

Sreekumar, P., & Khadkikar, V. (2017). Direct control of the inverter impedance to achieve controllable harmonic sharing in the islanded microgrid. IEEE Transactions on Industrial Electronics, 64(1), 827–837. DOI: 10.1109/TIE.2016.2574308.

Uddin, M., Mo, H., Dong, D., Elsawah, S., Zhu, J., & Guerrero, J. M. (2023). Microgrids: A review, outstanding issues and future trends. Energy Strategy Reviews, 49, Article 101127. DOI: 10.1016/j.esr.2023.101127.

Vasquez, J. C., Guerrero, J. M., Savaghebi, M., Eloy Garcia, J., & Teodorescu, R. (2013). Modeling, analysis, and design of stationary reference frame droop controlled parallel three-phase voltage source inverters. IEEE Transactions on Industrial Electronics, 60(4), 1271–1280. DOI:10.1109/TIE.2012.2194951.

Wang, L., Li, T., Cheng, Z., Hu, X., Li, Z., Liu, Z., Huang, J., & Hou, X. (2023). A unified droop control of AC microgrids under different line impedances: Revisiting droop control and virtual impedance method. Frontiers in Energy Research, 11, 1190833. DOI: 10.3389/fenrg.2023.1190833.

Wang, R., Hsu, S.‑C., Zheng, S., Chen, J.‑H., & Li, X. I. (2020). Renewable energy microgrids: Economic evaluation and decision making for government policies to contribute to affordable and clean energy. Applied Energy, 274, 115287. DOI: 10.1016/j.apenergy.2020.115287.

Wang, R., Zhao, X., Sun, Q., Xiao, J., Zhang, L., & Wang, P. (2023). Stability Analysis of Phase Locked Loops for AC Microgrids With Hybrid Power Sources. IEEE Transactions on Energy Conversion, 38(2), 1197–1207. DOI : 10.1109/TEC.2022.3224015.

Wu, D., Dragicevic, T., Vasquez, J. C., Guerrero, J. M., & Guan, Y. (2014). Secondary coordinated control of islanded microgrids based on consensus algorithms. IEEE Energy Conversion Congress and Exposition (ECCE), Pittsburgh, PA, USA, 4290–4297. DOI:10.1109/ECCE.2014.6953986.

Xu, J., & Xie, S. (2018). LCL-resonance damping strategies for grid-connected inverters with LCL filters: A comprehensive review. Journal of Modern Power Systems and Clean Energy, 6(2), 292–305. DOI: 10.1007/s40565-017-0319-7.

Yang, Y., & Blaabjerg, F. (2013). A new power calculation method for single-phase grid-connected systems. 2013 IEEE International Symposium on Industrial Electronics, Taipei, Taiwan. DOI:10.1109/ISIE.2013.6563684.

Yao, W., Yang, Y., Zhang, X., Blaabjerg, F., & Loh, P. C. (2017). Design and analysis of robust active damping for LCL filters using digital notch filters. IEEE Transactions on Power Electronics, 32(3). 2360–2375. DOI: 10.1109/ISIE.2013.6563684.